

The Distribution of Active Force Generators Controls Mitotic Spindle Position

Stephan W. Grill,^{1,2*} Jonathon Howard,^{1*} Erik Schäffer,¹
Ernst H. K. Stelzer,² Anthony A. Hyman¹

During unequal cell divisions a mitotic spindle is eccentrically positioned before cell cleavage. To determine the basis of the net force imbalance that causes spindle displacement in one-cell *Caenorhabditis elegans* embryos, we fragmented centrosomes with an ultraviolet laser. Analysis of the mean and variance of fragment speeds suggests that the force imbalance is due to a larger number of force generators pulling on astral microtubules of the posterior aster relative to the anterior aster. Moreover, activation of heterotrimeric guanine nucleotide-binding protein (G protein) α subunits is required to generate these astral forces.

Cell divisions creating daughter cells of unequal sizes are widespread in developing organisms, where they contribute to the generation of cell fate diversity (1). During such divisions, the mitotic spindle is off-center at the end of anaphase. The cleavage furrow then bisects the spindle in the middle, generating two daughter cells of unequal size (2). During the first division of a *C. elegans* embryo, the polarity of the cell is established after fertilization through the action of the *par* genes (3) and associated components (4–6). At metaphase, the mitotic spindle is positioned in the center of the cell, aligned along the anterior-posterior (AP) axis. At anaphase, the anterior pole remains in a fixed position, whereas the posterior pole moves toward the posterior cortex, resulting in an off-center spindle (7). Displacement of the spindle is caused by a larger net force acting on the posterior spindle pole than on its anterior counterpart (8).

An increase in net force on the posterior pole relative to the anterior one could be determined by differences in the number, strength, or distribution of force-generating interactions between the cell cortex and the astral microtubules that extend out from spindle poles toward the cortex (9, 10). These force-generating interactions could be driven by molecular motors or microtubule depolymerization (11–13). To measure the distribution of force generators, we devised an experiment to determine the spatial arrangement of the forces exerted on spindle poles by astral microtubules. We ablated the central region of the centrosome, causing the pericentriolar material to fragment and expand out toward

the cortex. We term this procedure optically induced centrosome disintegration (OICD).

After OICD, indirect immunofluorescence showed that separated aster fragments were radially distributed around the original location of the irradiated centrosome, whereas the unirra-

diated centrosome and its aster remained intact (Fig. 1, A and B). We followed the movement of aster fragments directly in a *C. elegans* strain containing green fluorescent protein (GFP)-tagged α -tubulin or indirectly by monitoring yolk granules close to the centrosome (14) (Fig. 2A). Both assays revealed the striking effect of OICD: After disintegration, the fragmented aster expanded out toward the cortex (Fig. 2, A to C) (fig. S2 and movies S1 to S4).

Late in anaphase, the anterior spindle pole remains relatively still, whereas the posterior spindle pole oscillates as it moves toward the cortex (7). We measured the OICD-triggered displacement of aster fragments as a function of direction for both asters at this time (14), because this is when the difference in speed between the anterior and posterior spindle poles is greatest. In the differential interference contrast (DIC) assay, typically 15 granules evenly distributed around the centrosome were tracked for each experiment (Fig. 2, B and C). In the GFP assay, microtubule-based structures were directly tracked. In both assays, the displacements over the initial 5 s after OICD were interpolated (14) to generate a curve describing the rate of expansion as a function of direction (figs. S3

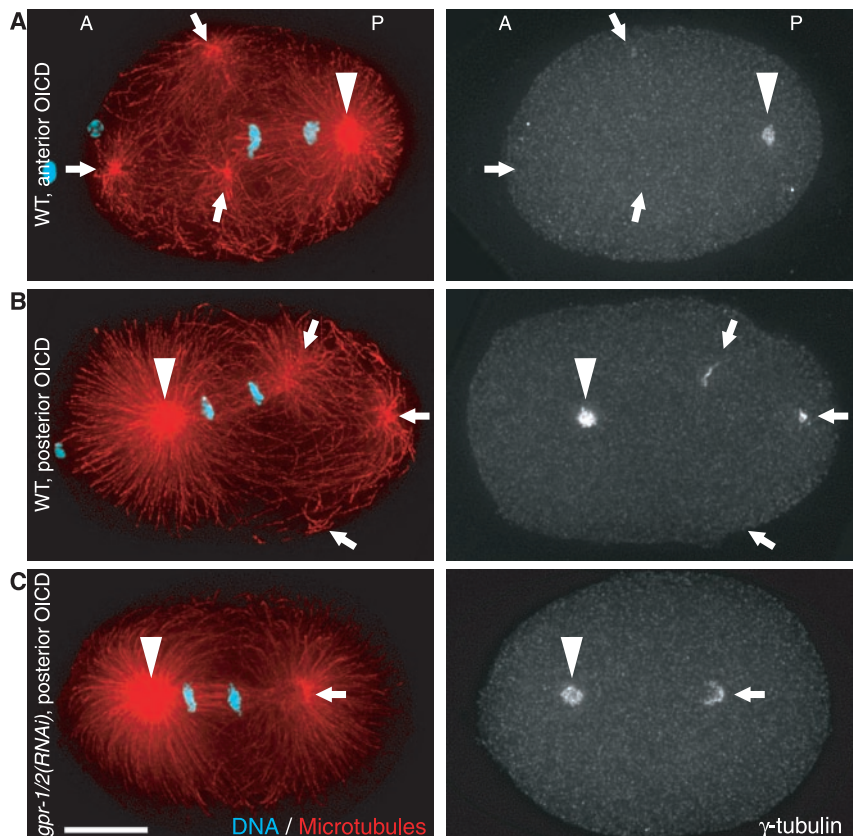


Fig. 1. OICD aster fragments. Microtubule asters and centrosomes were visualized by indirect immunofluorescence with antibodies to tubulin (red, left panels) and to γ -tubulin (right panels) (28). DNA is stained in blue (left panels). Anterior (A) is to the left, posterior (P) to the right, in this and all other figures. Arrows point to aster fragments, arrowheads to unirradiated centrosomes. (A) Anterior and (B) posterior OICD in wild-type (WT) embryos. Large fragments contained detectable levels of γ -tubulin (right panel, arrows) (29). (C) OICD in a *gpr-1/2(RNAi)* embryo does not cause aster fragmentation (right panel, arrow). Scale bar, 10 μ m.

¹Max Planck Institute of Molecular Cell Biology and Genetics, D-01307 Dresden, Germany. ²European Molecular Biology Laboratory, D-69117 Heidelberg, Germany.

*To whom correspondence should be addressed. E-mail: grill@mpi-cbg.de, howard@mpi-cbg.de

and S4). Means and SDs were calculated (30 DIC and 16 GFP experiments for both anterior and posterior OICD), resulting in an angular distribution of mean fragment speeds (Fig. 3, A and B) (fig. S1). Interestingly, fragment movement after OICD was not restricted to a particular angular range. Thus, the posterior movement of the mitotic spindle is not accomplished by confining force generators to a specific cortical region, but instead is due to distributed force generation (15).

The angular dependence of fragment velocities differed markedly between anterior and posterior OICD experiments. After OICD of the stationary anterior pole, fragment movement was symmetric about the AP axis. By contrast, after OICD of the oscillatory posterior pole, fragments traveling in the initial direction of movement of the pole moved at higher speeds than fragments traveling in the opposite direction (Fig. 2, B, C, F, and G; Fig. 3, A and B). Because cytoplasmic viscosity appears to be the same at the anterior and posterior (δ), and because anterior and posterior aster fragments were of the same size on average and the size of a fragment and the direction of movement were uncorrelated (Fig. 3A, inset), these differences in speed are likely due to the differences in the force acting on the aster fragments.

Higher forces could be due to more force generators per fragment or to a larger force per individual force generator. These possibilities can be distinguished by the analysis of the fluctuation in the speed of fragments from one experiment to the next. The variance in speed in any given direction initially increased as the mean speed increased, reached a maximum, and surprisingly decreased at high mean speeds (Fig. 3C). This nonlinearity was statistically significant (second-order coefficients were significantly different from 0; Student t test, $|t| > 10$, $P < 10^{-15}$). Whereas most sources of error are expected to cause a monotonic increase in variance (14), a decrease in variance is observed for two-state systems such as ion channels that are either open or closed. In this case, the current variance falls as all channels saturate in their open state (16). By analogy, our data suggest that a two-state process is acting to move aster fragments, and that the fall in variance is due to saturation of a limited number of active force generators that are pulling on the fragments.

The initial slopes of the mean-variance curves were similar for anterior and posterior experiments, but the anterior variance peaked at a lower speed (Fig. 3C). This can be interpreted by formulating a two-state

model in which each fragment interacts with N force generators on the cortex, and the speed of a fragment is proportional to the number of active force generators (in what we call the force-limited regime). The mean speed \bar{v} and the variance σ_v^2 are then given by

$$\bar{v} = Npv_c \quad (1)$$

$$\sigma_v^2 = Np(1-p)v_c^2 \quad (2)$$

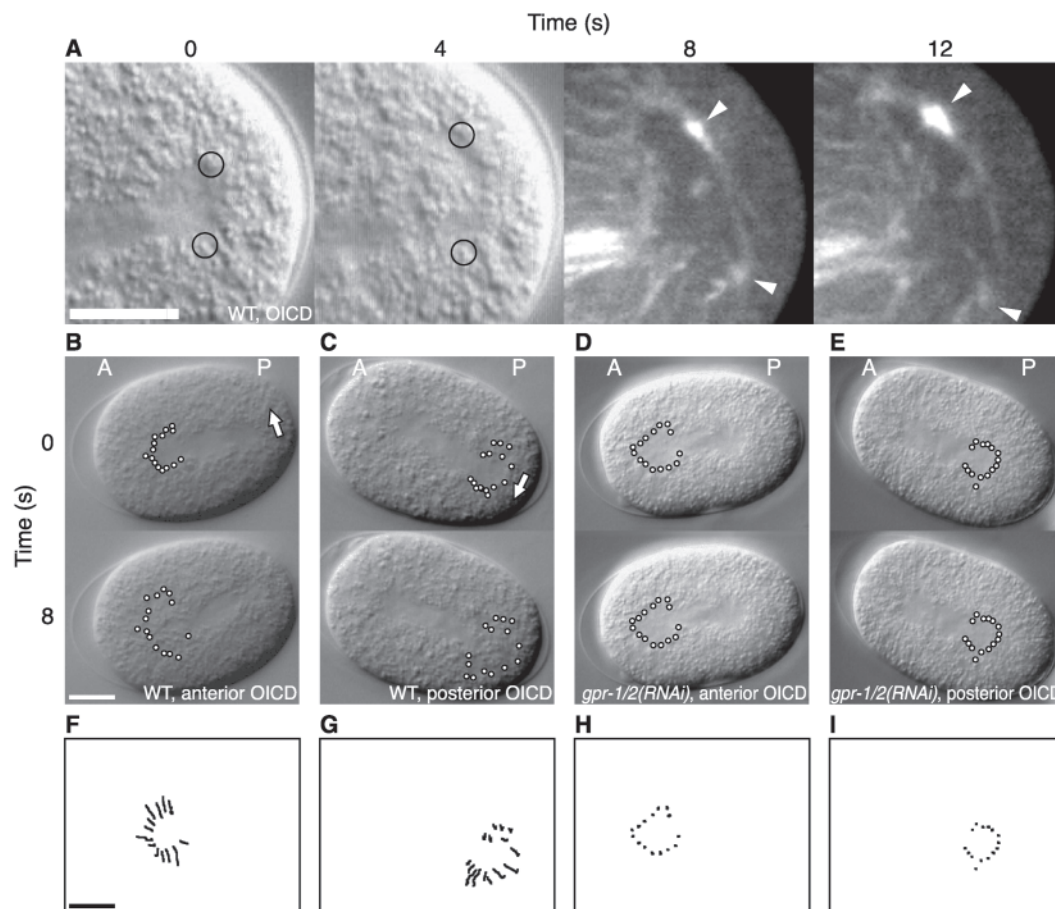
$$v^e = f\gamma^{-1} \quad (3)$$

(14, 16, 17), where v_c is the elementary speed due to a single force generator that exerts a force f , p is the probability of a force generator being in its active state, and γ is the drag coefficient of a fragment. Expressing the variance in terms of the mean speed results in a parabolic relationship,

$$\sigma_v^2 = v_c\bar{v} - (1/N)\bar{v}^2 \quad (4)$$

This equation provided a good fit to the data ($R^2 = 0.96$ for anterior and $R^2 = 0.94$ for posterior OICD, DIC assay; Table 1). Thus, a two-state model for force generators is consistent with the experimental data. Although our data do not favor any molecular mechanism, a microtubule-based motor such as dynein (18, 19) could be actively engaged with the end of a microtubule in one state, whereas it could be detached in the other.

Fig. 2. Movement of OICD aster fragments. (A) DIC and GFP image series of an embryo containing GFP- α -tubulin. At $t = 0$ s, OICD was performed; at $t = 8$ s, recording was switched from DIC to GFP. Circles indicate the positions of two yolk granules; arrowheads denote the aster fragments they follow. (B to E) Fragment movement in the DIC assay; displayed is an embryo directly after OICD ($t = 0$ s) and at $t = 8$ s. The positions of 15 granules distributed around the irradiated centrosome are indicated. (B) Anterior and (C) posterior OICD in WT embryos. Arrows indicate direction of movement of the posterior spindle pole before OICD. (D) Anterior and (E) posterior OICD in *gpr-1/2(RNAi)* embryo. (F to I) Respective trajectories of yolk granule positions. Scale bars, 10 μ m.



REPORTS

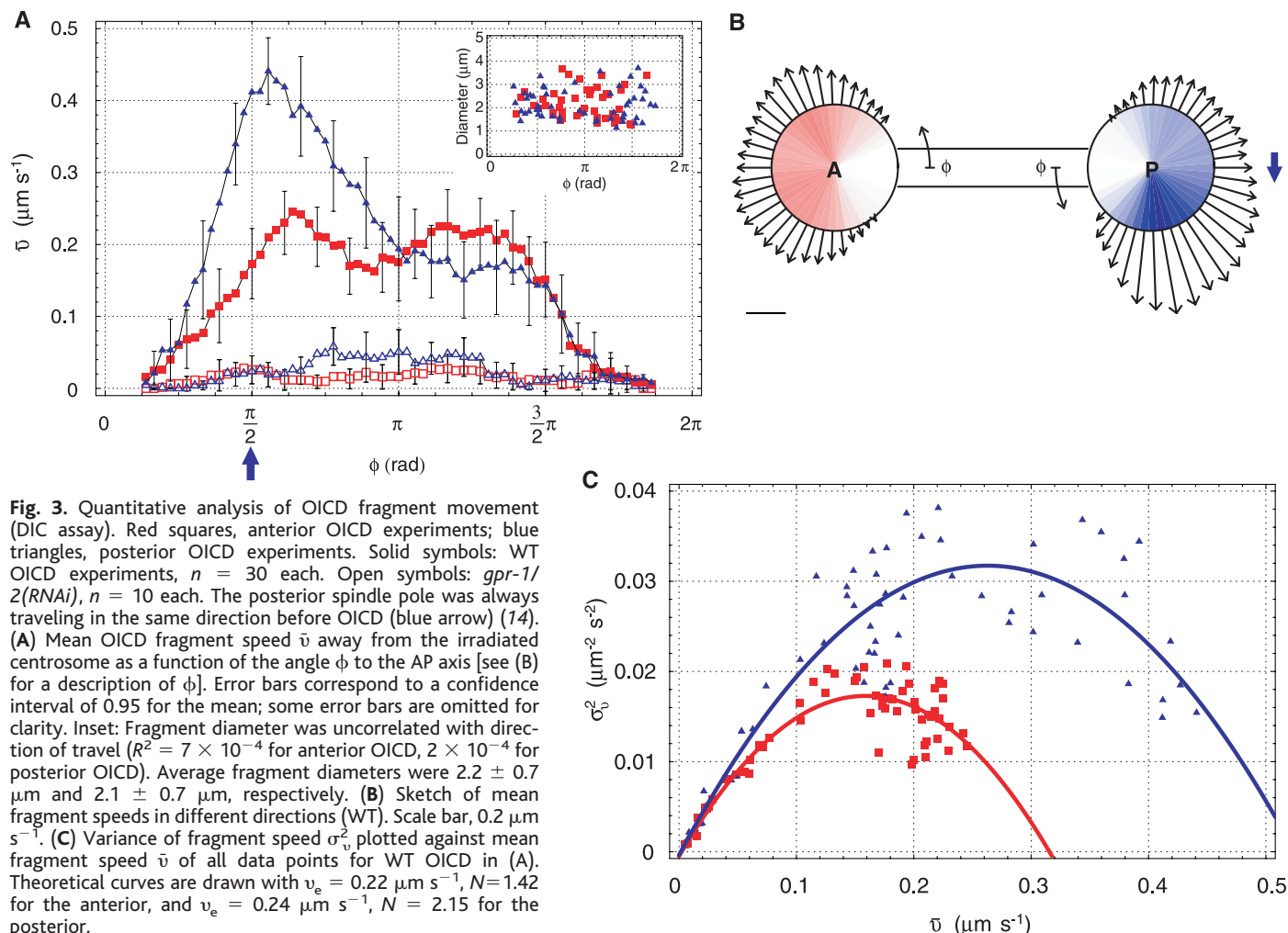


Fig. 3. Quantitative analysis of OICD fragment movement (DIC assay). Red squares, anterior OICD experiments; blue triangles, posterior OICD experiments. Solid symbols: WT OICD experiments, $n = 30$ each. Open symbols: *gpr-1/2(RNAi)*, $n = 10$ each. The posterior spindle pole was always traveling in the same direction before OICD (blue arrow) (74). (A) Mean OICD fragment speed \bar{v} away from the irradiated centrosome as a function of the angle ϕ to the AP axis [see (B) for a description of ϕ]. Error bars correspond to a confidence interval of 0.95 for the mean; some error bars are omitted for clarity. Inset: Fragment diameter was uncorrelated with direction of travel ($R^2 = 7 \times 10^{-4}$ for anterior OICD, 2×10^{-4} for posterior OICD). Average fragment diameters were $2.2 \pm 0.7 \mu\text{m}$ and $2.1 \pm 0.7 \mu\text{m}$, respectively. (B) Sketch of mean fragment speeds in different directions (WT). Scale bar, $0.2 \mu\text{m s}^{-1}$. (C) Variance of fragment speed σ_v^2 plotted against mean fragment speed \bar{v} of all data points for WT OICD in (A). Theoretical curves are drawn with $v_e = 0.22 \mu\text{m s}^{-1}$, $N = 1.42$ for the anterior, and $v_e = 0.24 \mu\text{m s}^{-1}$, $N = 2.15$ for the posterior.

Table 1. Fit parameters. The elementary speed v_e , the number of force generators per fragment N , the determination coefficient R^2 (30), the reduced χ^2 , and the corresponding one-sided probability of the χ^2 distribution (P) are given for anterior (A) and posterior (P) wild-type fragmentation experiments using the DIC and GFP assays (74). Deviations between assays were expected (37).

Assay		v_e ($\mu\text{m s}^{-1}$)	N	R^2	Reduced χ^2	P
DIC	A	0.22 ± 0.01	1.42 ± 0.11	0.96	0.60	0.18
	P	0.24 ± 0.01	2.15 ± 0.15	0.94	0.87	0.44
GFP	A	0.18 ± 0.01	1.91 ± 0.15	0.72	0.48	0.07
	P	0.18 ± 0.01	2.62 ± 0.29	0.91	0.93	0.48

The elementary speeds of anterior and posterior fragments were $0.22 \pm 0.01 \mu\text{m s}^{-1}$ and $0.24 \pm 0.01 \mu\text{m s}^{-1}$, respectively (DIC assay; Table 1). Because the sizes of fragments were the same and the viscosity is homogeneous, this equality of elementary speeds suggests that the elementary forces themselves are equal. We cannot reliably estimate the absolute value of the force because of uncertainty in the absolute value of the drag coefficient.

The similarity of the elementary speeds provides experimental evidence that the force generators are the same throughout the embryo (i.e., they have the same unitary force and velocity) and that differences in speeds of aster fragments are due to differences in the number of force

generators that are moving them. In agreement with this expectation, the average number of force generators for anterior and posterior fragments differed (1.42 ± 0.11 and 2.15 ± 0.15 , respectively, DIC assay; Table 1). The finding that N is greater than 1 supports our assumption that force generators are operating in the force-limited regime (20). Interestingly, the total number of active force generators is quite small, probably fewer than 50 (an exact number critically depends on the average number of fragments generated) (21). Because the total number of force generators is greater on the posterior than on the anterior side, we suggest that the force imbalance during spindle displacement (8) is due to an increase in the number of active

force generators rather than an increase in the elementary force.

The G protein α subunit ($G\alpha$) signaling pathway is required for spindle displacement (22, 23). OICD in *gpr-1/2(RNAi)* embryos, in which $G\alpha$ activity is inhibited and net forces on spindle poles are severely compromised (24–27), did not result in the expansion of aster fragments toward the cortex (Fig. 1C), and the mean fragment speeds were greatly reduced (14) (Fig. 2, D, E, H, and I; Fig. 3A). Therefore, spindle displacement is defective in the absence of $G\alpha$ activity because of a complete lack of active force generators. We suggest that the asymmetrically localized GPR-1/2 (25, 26) increases the pool of cortical protein complexes that are available to interact with the plus ends of the astral microtubules on the posterior side, ultimately leading to spindle displacement and unequal cleavage.

References and Notes

1. H. R. Horvitz, I. Herskowitz, *Cell* **68**, 237 (1992).
2. R. Rappaport, *Int. Rev. Cytol.* **31**, 169 (1971).
3. K. J. Kemphues, S. Strome, in *C. elegans II*, D. L. Riddle, T. Blumenthal, B. J. Meyer, J. R. Priess, Eds. (Cold Spring Harbor Laboratory Press, Cold Spring Harbor, NY, 1997), pp. 335–359.

Role of Subplate Neurons in Functional Maturation of Visual Cortical Columns

Patrick O. Kanold, Prakash Kara, R. Clay Reid, Carla J. Shatz*

The subplate forms a transient circuit required for development of connections between the thalamus and the cerebral cortex. When subplate neurons are ablated, ocular dominance columns do not form in the visual cortex despite the robust presence of thalamic axons in layer 4. We show that subplate ablation also prevents formation of orientation columns. Visual responses are weak and poorly tuned to orientation. Furthermore, thalamocortical synaptic transmission fails to strengthen, whereas intracortical synapses are unaffected. Thus, subplate circuits are essential not only for the anatomical segregation of thalamic inputs but also for key steps in synaptic remodeling and maturation needed to establish the functional architecture of visual cortex.

Subplate neurons, located in the developing white matter (WM), are among the first postmitotic cortical neurons (1). They are also first to receive functional synaptic inputs from the thalamus; their axons relay this input into the cortical plate well in advance of the invasion of thalamic axons into layer 4 (1). Once thalamic axons have arrived in layer 4, subplate neurons are gradually eliminated during the period of ocular dominance column (ODC) formation (1–3). Thus, subplate neurons are in a key, intermediate position to control the flow of information into the developing cortex when first spontaneous (prenatal) and then visual (postnatal) activity are present (3). Early subplate ablation prevents the invasion of thalamic axons into layer 4 (4), whereas later ablation blocks the anatomical segregation of thalamic axons from the lateral geniculate nucleus (LGN) into ODCs in primary visual cortex (5).

The prevailing hypothesis about ODC formation and plasticity is that activity-dependent competition between LGN axons representing each eye leads to their selective growth or pruning (3). However, recent observations that ODCs emerge earlier than previously thought, even before the onset of patterned visual experience (2, 6), have required a revision of this hypothesis, and one suggestion is that subplate neurons are involved (2).

To determine how the subplate might influence functional development and organization of visual cortex, subplate neurons were selectively ablated at P6 to P9 in cats (7). This time is just before the onset of ODC formation (6, 8, 9) and just after the

ingrowth of LGN axons to cortical layer 4 (10). To make localized and selective ablations, we either used kainic acid injections (4, 5) or an immunotoxin (11, 12) to p75, a neurotrophin receptor expressed in the neocortex only by subplate neurons at this age (1).

Response properties of cortical neurons were evaluated after subplate ablation by optical imaging and microelectrode recordings at P24 to P49 (7), when well-organized orientation maps are normally present (6, 13, 14). Orientation maps in control hemispheres or far from the ablation were highly organized (Fig. 1A, left and center), in contrast to poor organization in the highly local region surrounding the immunotoxin-ablated area (Fig. 1A, center). Kainic acid injections created even larger regions of disrupted or absent orientation maps (Fig. 1A, right). Polar maps representing both the angle and strength of tuning revealed weaker orientation selectivity in the ablated region (Fig. 1B), indicating the existence of an additional severe functional deficit. ODC maps were also degraded in ablated hemispheres (fig. S1), consistent with previous anatomical data (5).

Degraded orientation maps can result from neurons well tuned to different orientations but not segregated into columns, from neurons poorly tuned for orientation, or simply from neurons that respond poorly to visual stimuli. To distinguish between these alternatives, ocular dominance and orientation tuning of single cortical neurons were measured with microelectrode recordings (7) in both ablated and control regions in each animal (Fig. 1A and fig. S2). Because LGN axons are abundant in layer 4 of subplate-ablated cortex (Fig. 2A) (5), we had expected to find strong visually driven responses. Instead, there were fewer visually responsive units in the ablated area (15), and they were less orientation-selective.

4. R. Lyczak, J. E. Gomes, B. Bowerman, *Dev. Cell* **3**, 157 (2002).
5. J. Pelletier, G. Seydoux, *Science* **298**, 1946 (2002).
6. A. F. Severson, D. L. Baillie, B. Bowerman, *Curr. Biol.* **12**, 2066 (2002).
7. D. Albertson, *Dev. Biol.* **101**, 61 (1984).
8. S. W. Grill, P. Gönczy, E. H. K. Stelzer, A. A. Hyman, *Nature* **409**, 630 (2001).
9. D. J. Sharp, G. C. Rogers, J. M. Scholey, *Nature* **407**, 41 (2000).
10. P. Gönczy, *Trends Cell Biol.* **12**, 332 (2002).
11. T. J. Mitchison, E. D. Salmon, *Nature Cell Biol.* **3**, E17 (2001).
12. S. C. Schuyler, D. Pellman, *J. Cell Sci.* **114**, 247 (2001).
13. J. Howard, A. A. Hyman, *Nature* **422**, 753 (2003).
14. See supporting data on Science Online.
15. M. F. Tsou, W. Ku, A. Hayashi, L. S. Rose, *J. Cell Biol.* **160**, 845 (2003).
16. F. J. Sigworth, *Nature* **270**, 265 (1977).
17. F. J. Sigworth, *J. Physiol. (London)* **307**, 97 (1980).
18. D. Schmidt, S. Strome, unpublished data.
19. D. L. Dujardin, R. B. Vallee, *Curr. Opin. Cell Biol.* **14**, 44 (2002).
20. In the velocity-limited regime, a fragment moves at the maximum velocity whenever there are one or more force generators active. The more force generators per fragment, the higher the mean speed, because the probability of having at least one active force generator is increased. However, this model results in a mean-variance relationship identical to the force-limited case presented, with $N = 1$. This is not consistent with our results.
21. With fewer than 12 aster fragments generated per spindle pole and one or two active force generators per fragment, we expect fewer than 50 active force generators throughout the embryo at any time during anaphase.
22. M. Gotta, J. Ahringer, *Nature Cell Biol.* **3**, 297 (2001).
23. Y. Cai, F. Yu, S. Lin, W. Chia, X. Yang, *Cell* **112**, 51 (2003).
24. P. Gönczy *et al.*, *Nature* **408**, 331 (2000).
25. K. Colombo *et al.*, *Science* **300**, 1957 (2003); published online 15 May 2003 (10.1126/science.1084146).
26. M. Gotta, Y. Dong, Y. K. Peterson, S. M. Lanier, J. Ahringer, *Curr. Biol.* **13**, 1029 (2003).
27. D. G. Srinivasan, R. M. Fisk, H. Xu, S. Van Den Heuvel, *Genes Dev.* **17**, 1225 (2003).
28. E. Hannak *et al.*, *J. Cell Biol.* **157**, 591 (2002).
29. Because the laser was focused at regions where the pericentriolar material and γ -tubulin are localized, we expect a fraction of the centrosomal γ -tubulin to be destroyed. Consequently, not all aster fragments contained detectable levels of γ -tubulin.
30. L. Sachs, *Applied Statistics: A Handbook of Techniques* (Springer, New York, 1984).
31. Stray light from the pulsed ultraviolet (UV) laser used for OICD bleached the surrounding GFP- α -tubulin. Therefore, UV laser power was reduced by about 70% to visualize fragment movement by GFP. With less laser power, we probably produced larger fragments with an increased drag coefficient. Thus, elementary speeds were smaller in the GFP assay than in the DIC assay. On the other hand, larger fragments have more force generators associated, consistent with the general increase in N for the GFP assay.
32. We thank C. Cowan, A. Desai, M. Diehl, P. Gönczy, M. Glotzer, E. Hannak, F. Jülicher, K. Oegema, L. Pelletier, A. Riedinger, G. Ritter, E. Sackmann, N. Salmon, M. Srayko, and E. Tanaka for useful discussions, experimental assistance, and helpful comments. Supported by Deutsche Forschungsgemeinschaft grant SPP 1111 (HY3/2-1).

Supporting Online Material

www.sciencemag.org/cgi/content/full/301/5632/518/DC1

Materials and Methods

SOM Text

Figs. S1 to S7

References

Movies S1 to S7

7 May 2003; accepted 18 June 2003

Department of Neurobiology, Harvard Medical School, Boston, MA 02115, USA.

*To whom correspondence should be addressed. E-mail: carla_shatz@hms.harvard.edu